Numerical Simulation of One- and Two-Dimensional ESEEM Experiments

Z. L. Madi, S. Van Doorslaer, and A. Schweiger

Physical Chemistry, ETH Zurich, CH-8093 Zurich, Switzerland

E-mail: schweiger@esr.phys.chem.ethz.ch

Numerical simulation has become an indispensable tool for the interpretation of pulse EPR experiments. In this work it is shown how automatic orientation selection, grouping of operator factors, and direct selection and elimination of coherences can be used to improve the efficiency of time-domain simulations of one- and two-dimensional electron spin echo envelope modulation (ESEEM) spectra. The program allows for the computation of magnetic interactions of any symmetry and can be used to simulate spin systems with an arbitrary number of nuclei with any spin quantum number. Experimental restrictions due to finite microwave pulse lengths are addressed and the enhancement of forbidden coherences by microwave pulse matching is illustrated. A comparison of simulated and experimental HYSCORE (hyperfine sublevel correlation) spectra of ordered and disordered systems with varying complexity shows good qualitative agreement.   © 2002 Elsevier Science (USA)

Key Words: EPR; ESEEM; simulations; matched pulses.

INTRODUCTION

Electron spin echo envelope modulation (ESEEM) techniques are now used extensively to investigate paramagnetic systems (*1–4*). The standard ESEEM methods are the one-dimensional two-pulse and three-pulse ESEEM (*1–3*) and the two-dimensional HYSCORE (hyperfine sublevel correlation) experiments (*5*). One of the main bottlenecks in the interpretation of ESEEM data is still the lack of fast and general simulation programs. Direct determination of the parameters of the spin Hamiltonian from the line positions (frequencies) and intensities in experimental spectra is possible only for the simplest spin systems. In rare situations the parameters can be determined using nonlinear least-squares fitting. In most cases, however, the spin system is too complex so that a fully automatic determination of the numerous parameters is impossible due to the immense computational costs and ambiguous solutions. This is particularly true for disordered systems and for sophisticated multipulse EPR experiments. Stepwise correction of a set of trial parameters based on a repeated visual comparison of simulated and experimental spectra may then lead to the solution. Efficient and reliable spectral simulation software is a necessary prerequisite for the success of such a procedure.

Several approaches are feasible to address this problem. The echo amplitude in an ESEEM experiment may be evaluated using one of the commercial software packages or programs with implemented matrix computations (MATLAB (*6*), IDL (*7*), Mathematica (*8*)). The proven reliability and the complete documentations available make this approach attractive (*9*). Due to the inherent interpretative nature of these interactive programs a simple implementation of the modulation formulae often leads to a rather inefficient solution. An alternative procedure requires the additional effort of implementing optimized extension routines (so-called mex-files in the case of MATLAB), but once this is done the effort is rewarded by very satisfactory results.

In the past years some effort has been invested into the development of stand-alone programs for the simulation of ESEEM spectra. Although these programs are in general very efficient, they are often specialized to some particular classes of problems. A large number of simulations concentrating mainly on one-dimensional ESEEM techniques have been described (*10–14*). The version of the general spin Hamiltonian program MAGRES (*15*) that allows for orientation selection and has been extended for HYSCORE simulations uses only ideal microwave (mw) pulses. The approach of Benetis and Sornes (*16*) combines known theoretical tools to derive formulae for the eigenvalues and eigenvectors of the spin Hamiltonian to compute one- and two-dimensional ESEEM spectra quickly and allows for nuclei with $I > 1/2$. However, the simulation program assumes the nuclear quadrupole interaction to be much smaller than the hyperfine and the nuclear Zeeman interactions and includes only the secular part of the nuclear quadrupole interaction. The program TRYSCORE (*17*) makes use of an efficient frequency-domain simulation of HYSCORE spectra (time-domain data are also generated using the inverse Fourier transform) and also treats nonideal mw pulses. It is however restricted to spin systems with one or two ^{14}N or ^{1}H nuclei with axial hyperfine interactions and allows only the application of user-specified sets of orientations. Pöppl *et al.* (*18–20*) treat systems with $I > 1/2$ nuclei with an isotropic or axial **g** matrix. They include the nuclear quadrupole interaction using first-order perturbation theory and no orientation selection is implemented.

On the other hand there is a large tradition in the simulation of multipulse experiments in the field of NMR (*21–23*) and

specialized noncommercial freeware originally designed for the simulations of NMR spectra can in principle also be applied to problems in EPR. As an example, the object-oriented C++ software package GAMMA (24) contains most of the functionality required for the simulation of ESEEM spectra (Hamilton operators, pulse and time propagators, computation of expectation values, etc.). Although GAMMA is still mainly used for the simulation of NMR spectra, it has recently been successfully applied in the context of EPR spectroscopy (25–28).

In this paper a general strategy for the numerical simulation of ESEEM experiments in the time domain is given and it is shown how the computational efficiency can be improved. In particular we attempted to collect some of the most important features of existing approaches, extend them to larger spin systems with a varying number of quadrupolar nuclei, include an accurate automatic orientation selection scheme, and allow for the most general form of the various interactions, as well as avoid the use of approximate analytical expressions. Special attention is paid to the simulation of HYSCORE spectra. Spin simulations were performed using both GAMMA and MATLAB in order to compare the results and the performance of the different software packages. Comparisons between experimental and simulated HYSCORE spectra are made for systems with significant **g** anisotropy and nuclei with $I > 1/2$. Furthermore, the effect of the nonideality of the mw pulses on the HYSCORE spectra is discussed.

SIMULATION OF ESEEM EXPERIMENTS IN THE TIME DOMAIN

General Concepts

The echo intensity in an ESEEM experiment can be described using the density operator formalism (1, 2, 21, 29, 30). In the following we will focus on the HYSCORE experiment, $\pi/2-\tau-\pi/2-t_1-\pi-t_2-\pi/2-\tau$–echo (Fig. 1a), but all findings can be generalized to other ESEEM experiments. Denoting the pulse
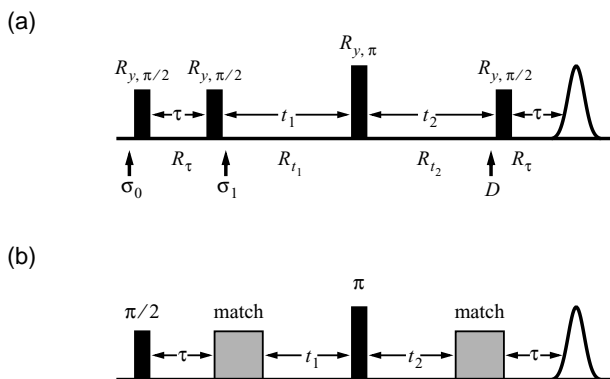

FIG. 1. Pulse sequences of the standard and matched HYSCORE experiments. (a) Standard HYSCORE and (b) matched HYSCORE. For the definition of the symbols see the text. The periods τ, t_1, and t_2 are free precession time intervals between the pulses.

propagators for a $\pi/2$ and a π pulse by $R_{\pi/2}$ and R_π, all representing rotations about the y axis of the rotating frame, and the time evolution operators by R_τ, R_{t_1}, and R_{t_2}, the echo amplitude of the HYSCORE experiment is given by

$$E(\tau,\ t_1,\ t_2) = \langle S_x \rangle(\tau,\ t_1,\ t_2)$$
$$= \mathrm{Tr}\big\{ R_\tau\, R_{\pi/2} R_{t_2} R_\pi R_{t_1} R_{\pi/2} R_\tau R_{\pi/2} \sigma_0 R_{\pi/2}^{-1} R_\tau^{-1}$$
$$\times\, R_{\pi/2}^{-1} R_{t_1}^{-1} R_\pi^{-1} R_{t_2}^{-1} R_{\pi/2}^{-1} R_\tau^{-1} S_x \big\},\qquad [1]$$

where σ_0 is the density operator at thermal equilibrium and S_x is the detection operator.

The numerical simulation of the HYSCORE experiment in the time domain consists of an efficient evaluation of $E(\tau, t_1, t_2)$ followed by the usual steps of data processing (baseline correction, filtration, and Fourier transformation).

When discussing the computational efficiency one should distinguish between the efficiency of the algorithm and the efficiency of the implementation. The latter issue is difficult to treat in a general way and, moreover, the programming languages used are developing and improving continuously. In this paper, we will mainly focus on how to improve the algorithms, but it is clear that the algorithms chosen should always be implemented as efficiently as possible. We made use of both the GAMMA and the MATLAB program. The object-oriented C++ software package GAMMA (24) contains most of the functionality needed for the simulations. On the other hand, MATLAB (6) allows the use of interactive user interfaces and MATLAB programs are generally very reliable and easily readable. The computational speed of user-defined functions can be further improved by implementing optimized extension routines written in C or FORTRAN.

Evaluation of the Echo Amplitude

The speed limiting step in the evaluation of the echo amplitude of an ESEEM experiment for a single observer position is the calculation and application of the propagators. It is clear that an algorithm in which Eq. [1] is straightforwardly implemented is not very efficient. The time needed for the calculation of the echo intensity can however be minimized by taking into account the following points.

First of all, the free evolution periods can be implemented in the eigenbasis of the spin Hamiltonian. By default, the matrix representation of an operator is set up in the Zeeman basis of the electron and nuclear spins. Since the matrix representation of the spin Hamiltonian in this basis contains off-diagonal elements, most of the propagators are represented by full matrices. The computational cost of the evaluation of a single time evolution step $\sigma_{t+\Delta t} = R\sigma_t R^{-1}$ is therefore proportional to n^3, where n is the number of states of the spin system. As described already in Ref. (31) in the eigenbasis U_0 of the static Hamiltonian $\mathcal{H}_0$ all the propagators $R^U = \mathrm{diag}(e^{i\omega_1 \Delta t}, \ldots, e^{i\omega_n \Delta t})$ are diagonal. Since these operations consist of only multiplying the rows and

columns of the matrix representation of the density operator by scalars, the time cost of the evaluation of a single time evolution step reduces to n^2,

$$\sigma_{t+\Delta t}^{U_0} = \text{diag}(e^{i\omega_j \Delta t})\sigma_t^{U_0}\text{diag}(e^{-i\omega_j \Delta t}) \qquad [2]$$

with $\sigma_t^{U_0} = U^{-1}\sigma_t U$.

Second, the repetitive evaluation of expectation values of observables in the eigenbasis of the Hamiltonian can be further restricted to density operator components (coherences) and detection operator elements of sufficiently high amplitude. The expectation value of an effective detection operator D evaluated in the eigenbasis U_0 of the Hamiltonian as a function of the time is given by

$$\langle D \rangle (t) = \sum_{jk} D_{jk}^{U_0}\sigma_{kj}^{U_0}e^{-i(\omega_k - \omega_j)t}. \qquad [3]$$

Since the exponential factor $e^{-i(\omega_k - \omega_j)t}$ has a constant unit modulus the summation must include only terms with an absolute value of $D_{jk}^{U_0}\sigma_{kj}^{U_0}$ above a certain threshold. This drastically reduces the number of matrix elements to be taken into account to the electron single-quantum coherences with large amplitude.

A significant further speedup can be obtained in some cases by a careful grouping of the remaining full matrix multiplications (32). For the HYSCORE experiment, for example, Eq. [1] can be rearranged to

$$E(\tau, t_1, t_2) = \langle S_x \rangle(\tau, t_1, t_2)$$
$$= \text{Tr}\{R_M R_{t_1}\sigma_1 R_{t_1}^{-1} R_M^{-1} R_{t_2}^{-1} D R_{t_2}\} \qquad [4]$$

with the mixing propagator $R_M = R_\pi$, the effective starting density operator

$$\sigma_1 = R_{\pi/2} R_\tau R_{\pi/2}\sigma_0 R_{\pi/2}^{-1} R_\tau^{-1} R_{\pi/2}^{-1}, \qquad [5]$$

and the effective detection operator (for notation see Fig. 1)

$$D = R_{\pi/2}^{-1} R_\tau^{-1} S_x R_\tau R_{\pi/2}. \qquad [6]$$

The parts independent of t_1 and t_2 can be precalculated saving further computer time. This procedure cannot be applied for experiments using two evolution intervals of simultaneously incremented lengths separated by some pulses and free evolution periods. Examples of such experiments are two-dimensional three-pulse ESEEM (33), spin-locked ESEEM (34), one- and two-dimensional sum combination-peak experiments (3, 28, 35), and the five-pulse ESEEM experiment introduced by Pöppl et al. (36).

Finally, elimination of undesired density operator components such as transverse electron magnetization during the evolution time in experiments using nuclear coherences (coherence selection) is possible simply by explicit weighting of coherences; a repetitive evaluation implementing phase cycles is not required. Suppression of electron coherences, for example, is realized by zeroing all elements of the density matrix which connect states in the spin system with different m_S values (32).

The general structure of simulations performed in the time domain is illustrated by the GAMMA and MATLAB code segments displayed in Table 1. These programs implement the evaluation of the echo amplitude based on Eq. [4].

Orientational Averaging

The majority of the samples studied by EPR are frozen solutions or powders. Such samples contain randomly oriented paramagnetic species and the observed spectrum is the sum of the spectra of the different subensembles. The total simulation time will be strongly affected by the efficiency of the powder averaging. The first step in the design of an ESEEM simulation procedure for a disordered system is the choice of the integration algorithm. The accuracy of various integration algorithms has been tested (37) and they were found to have similar performance, provided that there are no systematic errors influencing the results, such as carrying out the integration in a coordinate system other than the principal axes system of the **g** matrix. We chose an algorithm which distributes a number of base points along the latitudes of the unit sphere proportional to the length of the latitude (sinusoidal projection). The speed and accuracy of this simple and efficient integration method are reported to be very satisfactory (37).

Since the anisotropy of the **g** matrix and the hyperfine interactions often exceed the amplitude of the available mw field, only a narrow window of the EPR spectrum can be excited simultaneously by the pulse sequence. This in turn corresponds to a subset of species in a disordered system with coinciding orientations. Numerical calculations however are often simplified by the assumption of ideally nonselective pulses, i.e., pulses of length zero and infinite strength, which excite the whole EPR spectrum uniformly. This problem may be solved as follows: (a) All orientations contributing to the EPR spectrum are considered, but only the **g** matrix and hyperfine interactions with a magnitude at least comparable to the mw field strength are included. (b) Assuming a Gaussian excitation profile to account for both the frequency distribution of the nearly rectangular pulse and the variation of the static B_0 field strength over the sample in the cavity and other imperfections, a weight depending on the difference between the resonance frequency of a spin packet and the applied mw frequency is assigned to each orientation. (c) The actual simulation is executed only for orientations with a weight above a certain preset cutoff value.

This procedure is a variant of the "orientation selection principle," introduced by Rist and Hyde (38–40) and used extensively for the simulation of ENDOR spectra of disordered systems (41–45), which we adopted for HYSCORE simulations. For most programs the orientations must be specified explicitly (17), which may also be less accurate. Orientation selection

TABLE 1
Code Fragments Illustrating the Use of GAMMA and MATLAB for the
Simulation of Two-Dimensional Echo Modulation

C++

```
S=−Iz(sys,0);                          // thermal equilibrium
S=evolve(S,Iy(sys,0),0.25);            // 1st pulse
S=evolve(S,H,tau);                     // tau evolution
S=evolve(S,Iy(sys,0),0.25);            // 2nd pulse
D=Ix(sys,0);                           // detection operator
D=evolve(D,H,−tau);                    // tau evolution backwards
D=evolve(D,Iy(sys,0),−0.25);           // 4th pulse
for (j=0;j<m;j++){                     // t1 loop
  S1=evolve(S,Iy(sys,0),0.50);         // 3rd (mixing) pulse
  FID(S1,D,H,dt,m,x);                  // echo sequence
  for(k=0;k<m;k++)spec(j,k)=x(k);      // accumulation
  S=evolve(S,H,dt);                    // t1 evolution step
};
```

MATLAB

```
R1=expm(−i*Sy*pi/2);                   % 90deg pulse
R2=expm(−i*Sy*pi);                     % 180deg pulse
Rt=expm(−i*2*pi*H*tau);                % time evolution
R=expm(−i*2*pi*H*dt);                  % time increment
S=−Sz;                                 % thermal equilibrium
S=R1*S*R1';                            % 1st pulse
S=Rt*S*Rt';                            % tau evolution
S=R1*S*R1';                            % 2nd pulse
D=Sx;                                  % detection operator
D=Rt'*D*Rt;                            % tau evolution backwards
D=R1'*D*R1;                            % 4th pulse
for j=1:m;                             % t1 loop
  S1=R2*S*R2';                         % 3rd (mixing) pulse
  spec(j,:)=FID(S1,D,R,m);             % echo sequence
  S=Rt*S*Rt';                          % t1 evolution step
end;
```

Note. H, Hamiltonian; S, density matrix; D, detection operator.

results in a substantial saving in computer time and is utilized also in the case of real pulses, i.e., pulses with finite amplitude and duration. Figure 2 shows the weights of the orientations in a disordered system with a rhombic **g** matrix with principal values 1.8, 2.0, and 2.2. The orientations with an effective g value of 2.0 are selected assuming a Gaussian lineshape with a FWHH of 235.5 MHz. The figure clearly illustrates that many of the orientations can be left out for the calculation of ESEEM spectra at this observer position.

Simulations with Real Pulses

For most ESEEM experiments, the pulses cannot be approximated by ideal pulses. In fact, a number of experiments (e.g., matched ESEEM (*26, 46–49*)) benefit from the use of tailored nonideal pulses. Consequently, the effect of the nonideality of the pulses should be considered in the simulations (*17, 50*). The time evolution during the extended mw irradiation periods (real pulses) is computed in a frame rotating with the mw frequency about the effective quantization axis of the electron spin. In the case of anisotropic **g** matrices the effective mw field is no longer

perpendicular to the static field. The components of the $\boldsymbol{B}_1$ field parallel to the effective static field modulate the energy levels of the system on a time scale which is much too short to be relevant for the observation of the echo signal. Therefore only the projection of the $\boldsymbol{B}_1$ field onto the plane perpendicular to the effective static field is considered in the calculations. The Hamiltonian during a pulse in the rotating frame is given by (*26*)

$$\mathcal{H}_1 = \mathcal{H}_0 + \omega_1(S_x \cos \varphi + S_y \sin \varphi), \qquad [7]$$

where ω_1 is the amplitude and φ is the phase of the applied mw field.

In an actual experiment the durations and amplitudes of the mw pulses are set by maximizing the echo amplitude in a two-pulse echo experiment. The effective g value relevant at a given frequency is in most cases not known. Moreover, due to the anisotropy of the various interactions, a large number of orientations with different properties contribute to the echo at the same mw frequency, so that the exact value of the mw field strength is also an unknown parameter. Misadjustment of the field strength
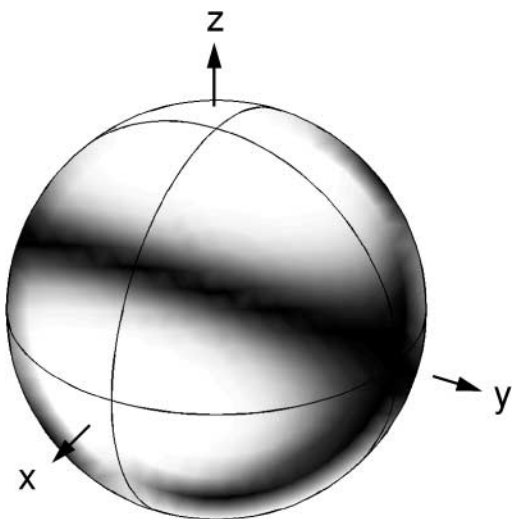
FIG. 2. Weights of orientations in a disordered system with a rhombic **g** matrix ($g_x = 1.8$, $g_y = 2.0$, and $g_z = 2.2$). Orientations with an effective g value of 2.0 are selected assuming a Gaussian EPR lineshape with a FWHH of 235.5 MHz. The grayscale indicates the weights of orientations; darker areas on the surface of the unit sphere correspond to higher weights, and white areas are ignored in the simulation.

leads to significant errors in the resulting pulse flip angles and thereby to the appearance of strong artifacts, such as large diagonal peaks, in the simulated spectra like in an experiment with inaccurately calibrated mw pulses.

A practical solution of this problem is to implement the experimental pulse calibration scheme by simulating a two-pulse echo experiment, $\pi/2-\tau-\pi-\tau-$echo, applied to a disordered system and determining the mw field strength corresponding to the maximum echo amplitude. Such a simulation involves only the electron spin and the most strongly coupled nuclei. When using mw pulses of finite length the echo maximum no longer appears at time τ after the second pulse, but is delayed by about half the length of the first pulse, and the shape of the echo is a complicated function of the spin Hamiltonian parameters (*1*). It is therefore necessary to display the echo amplitude as a function of the time t after the second pulse in addition to the B_1-field dependence. An example for this procedure is shown in Fig. 3 for an $S = 1/2$, $I = 7/2$ (^{59}Co) system. The adjustment should always be done at a B_0-field value which corresponds to the experiment. In the example the field strength for optimum echo amplitude is found to be $\omega_1/2\pi \approx 25$ MHz.

This procedure also allows one to treat enhanced electron-nuclear coherence transfers through forbidden transitions using matched mw pulses. The rather involved theory of microwave pulse matching is developed in full detail in Refs. (*26, 46–49*). It has been shown experimentally (*47*) that the use of matched pulses in HYSCORE experiments ($\pi/2-\tau-$matched$-t_1-\pi-t_2-$matched$-\tau-$echo, Fig. 1b) leads to a large increase in signal intensity. The corresponding improvement in the signal-to-noise ratio is often overwhelming for nuclei with a small modulation depth parameter k, as, for example, for strongly coupled nuclei
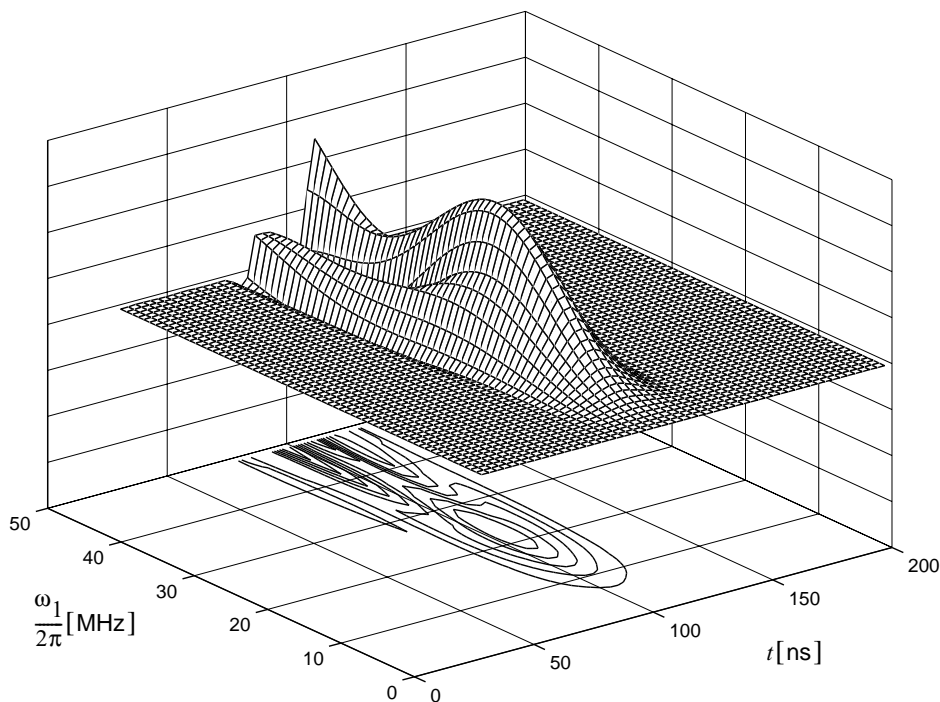

FIG. 3. Microwave field strength calibration by simulating a two-pulse echo for an electron-^{59}Co spin system with $t_{\pi/2} = 10$ ns, $t_\pi = 20$ ns, $\tau = 100$ ns; $g_x = 2.324$, $g_y = 2.324$, and $g_z = 2.087$; and $A_x^{Co} = 39$ MHz, $A_y^{Co} = 39$ MHz, $A_z^{Co} = 236.7$ MHz, and $B_0 = 332.4$ mT. The time t is measured from the end of the second pulse. The optimum field strength is found at about 25 MHz.

with a predominantly isotropic hyperfine interaction or weakly dipolar-coupled nuclei.

Starting from electron polarization neither an ideal selective nor an ideal nonselective pulse can generate nuclear coherence. However, since nuclear coherence can be generated by a real pulse of finite length, there exists an optimum mw field strength for the generation of such coherence. The transfer is governed by flip-flop terms proportional to the operator $S^+I^- + S^-I^+$ in the rotating-frame Hamiltonian and is most efficient when the mixing of the states connected by the flip-flop term is maximal; i.e., the states are degenerate (1, 26, 46). For an $S = 1/2$, $I = 1/2$ system the strength of the matching field in the weak-coupling case ($|A| < 2|\omega_I|$) (1) is given by

$$\omega_1^m = \frac{1}{|\omega_+/2| \cos \eta} \sqrt{\omega_\alpha \omega_\beta \left(\frac{\omega_+^2}{4} - \Omega_S^2 \right)}, \qquad [8]$$

where $\omega_+ = \omega_\alpha + \omega_\beta$ and η is the half angle between the quantization axis of the nucleus in the two electron manifolds, Ω_S is the resonance offset frequency of the electron spin, $\omega_{\alpha,\beta} = \sqrt{(\omega_I \pm A/2)^2 + (B/2)^2}$ are the basic nuclear frequencies, and ω_I is the nuclear Zeeman frequency.

In the strong-coupling case ($|A| > 2|\omega_I|$) (1) and assuming that the isotropic part of the hyperfine interaction is much larger than the anisotropic part, the mw field strength ω_1^m satisfying the matching condition is given by (1, 47)

$$\omega_1^m = \frac{1}{|\omega_I|} \sqrt{\left(\frac{A^2}{4} - \omega_I^2 \right) \left(\Omega_S^2 - \omega_I^2 \right)}. \qquad [9]$$

This condition is fulfilled by electron spins with offset Ω_S^m determined by

$$\left| \Omega_S^m \right| = |\omega_I| \sqrt{1 + \frac{\omega_I^2}{(A^2/4 - \omega_I^2)}}. \qquad [10]$$

The largest enhancement of forbidden transfers is obtained with the maximum available mw field strength (1).

Figures 4a and 4b show simulated HYSCORE spectra of an $S = 1/2$, $I = 1$ (^{14}N) system with $g = 2$, the hyperfine principal values $A_x^N = 51.96$ MHz, $A_y^N = 42.1$ MHz, $A_z^N = 43.64$ MHz, and the nuclear quadrupole principal values $Q_x^N = -1.71$ MHz, $Q_y^N = 1.91$ MHz, $Q_z^N = -0.2$ MHz for a standard HYSCORE experiment ($\pi/2$–τ–$\pi/2$–t_1–π–t_2–$\pi/2$–τ–echo) (a), and a HYSCORE experiment with matched pulses of length 72 ns and a mw field of $\omega_1/2\pi = 31.25$ MHz (b). Almost an order of magnitude enhancement of the cross peaks involving single-quantum (SQ) nuclear transition frequencies can be seen in the matched experiment in agreement with earlier
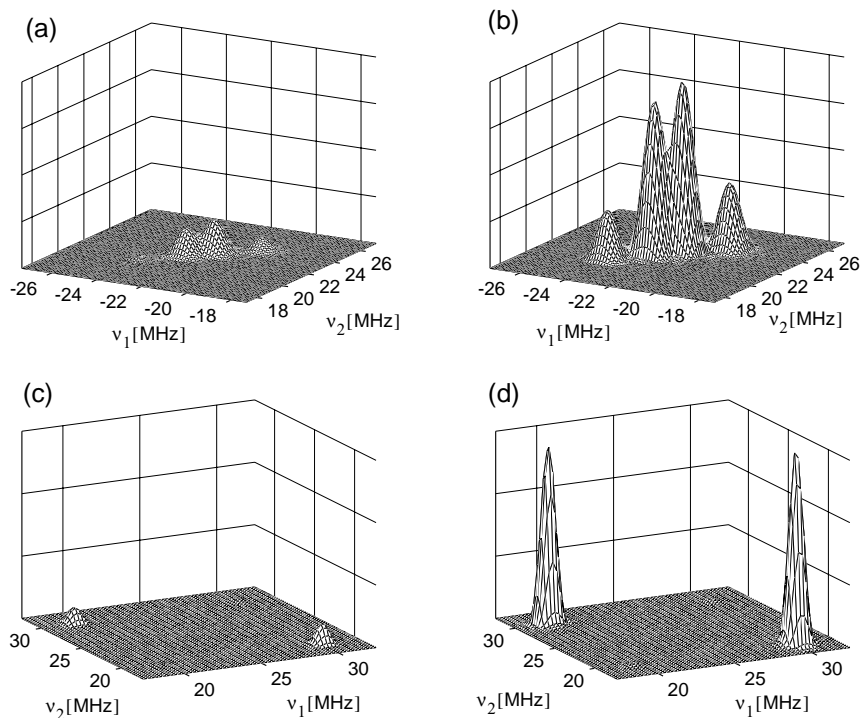

FIG. 4. Standard and matched HYSCORE. (a, b) HYSCORE simulations of a system with one unpaired electron interacting with a strongly coupled nitrogen nucleus, showing the SQ nuclear frequency region of the spectrum (simulation parameters, see text; an identical but arbitrary scaling of the amplitudes is used). Standard HYSCORE (a). Nitrogen-matched HYSCORE (b). (c, d) HYSCORE simulations of a system with one unpaired electron interacting with two weakly coupled protons, showing the DQ nuclear frequency region (simulation parameters, see text). Standard HYSCORE (c). Proton-matched HYSCORE (d).

experimental observations for nitrogen-matched HYSCORE of a single crystal of bis(salicylaldoximato)Ni(II), Ni(sal)$_2$, doped with Cu(sal)$_2$ (nitrogen hyperfine and nuclear quadrupole data are similar to the parameters used in the simulation) (*47*).

In the weak-coupling case (and assuming also $\Omega_S \ll \omega_I$) the condition of Eq. [8] simplifies to $\omega_1^m = |\omega_I|$ (*47*). During the strong, almost on-resonant irradiation of the electron spins the resonance frequency of the electron spins in the rotating frame is approximately ω_1, and due to hyperfine decoupling that of the nuclear spins is essentially ω_I. This results in a maximum rate of flip-flop transitions, i.e., in a maximum electron–nuclear polarization transfer. Generation of nuclear coherence also requires a change of the effective quantization axis of the nuclear spins, again ensured by the hyperfine decoupling effect. This change is maximal for complete decoupling: $\omega_1 \to \infty$. The matching field optimizes all forbidden processes which require nuclear spin flips. Matching in the weak-coupling case is achieved experimentally by adjusting the mw field strength near to the nuclear Zeeman frequency: $\omega_1 \approx |\omega_I|$ (*47*).

Figures 4c and 4d show the simulation of standard and matched proton HYSCORE spectra of an $S = 1/2$, $I_1 = 1/2$, $I_2 = 1/2$ system with $g = 2$, $A_x^H = 6.6$ MHz, $A_y^H = -0.87$ MHz, $A_z^H = -5.97$ MHz, and matched pulses of 72 ns and a mw field of $\omega_1/2\pi = 14.7$ MHz. A significant enhancement of the peaks in the double-quantum nuclear frequency (DQ) region of the spectrum is obtained. This finding is again corroborated by earlier experimental observations for the proton HYSCORE signals of Cu(sal)$_2$ (*47*). A highly sensitive experiment which makes use of matched pulses and is free of blind spots is SMART HYSCORE (matched–t_1–π–t_2–matched–τ–π–τ–echo) (*48, 49*).

SIMULATION OF ESEEM EXPERIMENTS IN THE FREQUENCY DOMAIN

The ESEEM spectrum is related to the time-domain echo modulation signal through Fourier transformation. For a two-dimensional experiment the spectrum can be expressed in the eigenbasis U_0 of the unperturbed Hamiltonian $\mathcal{H}_0$ as

$$E(\tau, \omega_1, \omega_2) = \sum_{j,k,l,m} \left(P_M^{U_0}\right)_{jk} \left(\sigma_1^{U_0}\right)_{kl} \left(P_M^{U_0}\right)_{ml}^* D_{mj}^{U_0}$$
$$\times (A_{kl}(\omega_1) - i B_{kl}(\omega_1))(A_{mj}(\omega_2) - i B_{mj}(\omega_2)),$$
$$[11]$$

where $A_{pq}(\omega) = A(\omega - \omega_{pq})$ is the absorption and $B_{pq}(\omega) = B(\omega - \omega_{pq})$ is the dispersion lineshape at the transition frequency ω_{pq}. Several ESEEM simulation approaches (*15, 17*) start with the calculation of the ESEEM frequencies. The spectrum is represented as a sum of δ functions positioned at the points of a frequency lattice with the complex amplitudes given in Eq. [11]. This spectrum is then convoluted with the desired lineshape. As long as the dimension of the

Hilbert space of the spin system is moderate, this simulation algorithm is very efficient.

In this work, programs were developed for the simulation of HYSCORE spectra in the time as well as in the frequency domain. Although the results should be strictly identical comparison of the spectra of disordered systems simulated with the same spin Hamiltonian parameters in the time and frequency domain show some minor differences. They are caused by the fact that in the frequency-domain case the line positions are restricted to points of a discrete grid so that the interference of spectral features with nearly identical frequencies and slightly different phases is represented with some distortions. In contrast, in the time domain frequencies are not restricted by the resolution of a finite grid consisting of at best a couple of hundred points, and the interference effects of overlapping spectral features are represented with high accuracy. Suitable numerical interpolation procedures may improve the faithfulness of the representation of spectra generated directly in the frequency domain and also increase the speed of the computation. These problems and possible remedies, as well as numerous other aspects of simulations of ESEEM spectra in the frequency domain, will be discussed in detail in Ref. (*51*).

A quick overview of all the possible frequencies in a HYSCORE spectrum can be obtained if one simplifies the above frequency-domain calculation by assigning a zero or unit amplitude to each grid position (ω_{kl}, ω_{mj}), and omitting the final convolution step. All four quadrants of such a representation contain identical information, as was recognized earlier (*52*). Figure 5 shows the possible frequencies in the HYSCORE spectrum of an $S = 1/2$, $I = 1$ system with $g = 2$, $A_x^N = 3.2$ MHz, $A_y^N = 2.4$ MHz, $A_z^N = 2.7$ MHz, and $(e^2qQ)/h = 1.69$ MHz, $\eta = |(Q_x - Q_y)/Q_z| = 1$ with $|Q_x| < |Q_y| < |Q_z|$ and with the quadrupole tensor rotated about the y axis by $\beta = 90°$ (second Euler angle). In the spectrum we recognize 2×9 ridges, which correspond to the nine possible
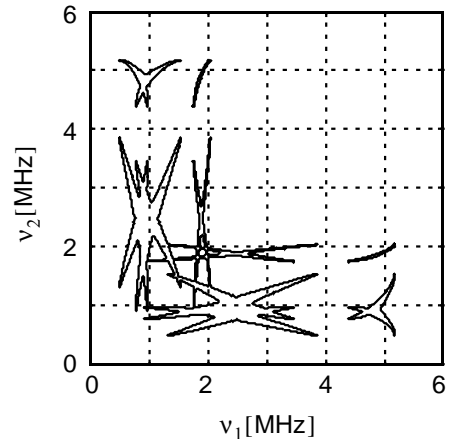

FIG. 5. Example of a fast simulation method giving all possible HYSCORE peak positions for an $S = 1/2$, $I = 1$ system (simulation data, see text).

combinations between the three nuclear frequencies of the α and the β manifold (two SQ and one DQ frequency for each m_S manifold). The procedure outlined can substantially reduce the time needed for the analysis of ESEEM spectra and may be helpful to get a first guess on the magnetic parameters of the system under investigation very rapidly (the computation including 16200 orientations requires 35 s on a 300-MHz SUN SPARC Ultra 10 computer). In contrast to earlier similar procedures (*17, 52, 53*) our approach allows for the inclusion of a variable number of quadrupolar nuclei and general (nonaxial) tensors and interaction matrices. The final step, however, should always be the full simulation of the ESEEM spectrum.

COMPARISON OF SIMULATED HYSCORE SPECTRA WITH EXPERIMENTAL DATA

Materials and Methods

Oxygenated cobalt(II) [^{15}N]tetraphenylporphyrin(pyridine) ((oxyCo)[^{15}N]TPP(py)) was prepared as described earlier (*54*). RbCl:O_2^- single crystals were obtained as in (*55*).

The HYSCORE spectra (measured at 15 K throughout) were recorded on a Bruker ESP 380 spectrometer (mw frequency, 9.71 GHz) equipped with a liquid helium cryostat from Oxford Inc. The magnetic field was measured with a Bruker ER 035 M NMR Gaussmeter. A repetition rate of 1 kHz was used. The experiments were carried out with the pulse sequence $\pi/2–\tau–\pi/2–t_1–\pi–t_2–\pi/2–\tau$–echo, with pulse lengths $t_{\pi/2} = 24$ ns and $t_\pi = 16$ ns. For the HYSCORE spectrum of (oxyCo)[^{15}N)TPP(py) the time intervals t_1 and t_2 were varied from 96 to 8272 ns in steps of 16 ns. Three τ values (96, 176, and 344 ns) were used to remove the blind spots. The observer position was $B_0 = 342.0$ mT. For the HYSCORE spectrum of RbCl:O_2^- the time intervals t_1 and t_2 were varied from 96 to 6160 ns in steps of 16 ns and the τ value was taken to be 96 ns. The observer position was chosen to be close to the [110] axis ($B_0 = 302.9$ mT).

Data processing was done with MATLAB (*6*). The time-domain data were baseline corrected with a third-order polynomial, apodized with a Hamming window, and zero-filled. After 2D Fourier transformation, the absolute-value spectra were calculated. To eliminate blind spots, the spectra measured at different τ values were added together. The simulated spectra were processed the same way.

Experiments versus Simulations

ESEEM techniques, especially three-pulse ESEEM and HYSCORE, are used to investigate weakly coupled nitrogens in metalloproteins and their model systems (*4*). Often, no single crystals can be grown, so that the experiments have to be done on frozen solutions. Figure 6a shows a HYSCORE spectrum of a frozen toluene solution of the heme model compound (oxyCo)[^{15}N)TPP(py) (*54*) taken at an observer position where several orientations contribute to the HYSCORE spectrum. Be-
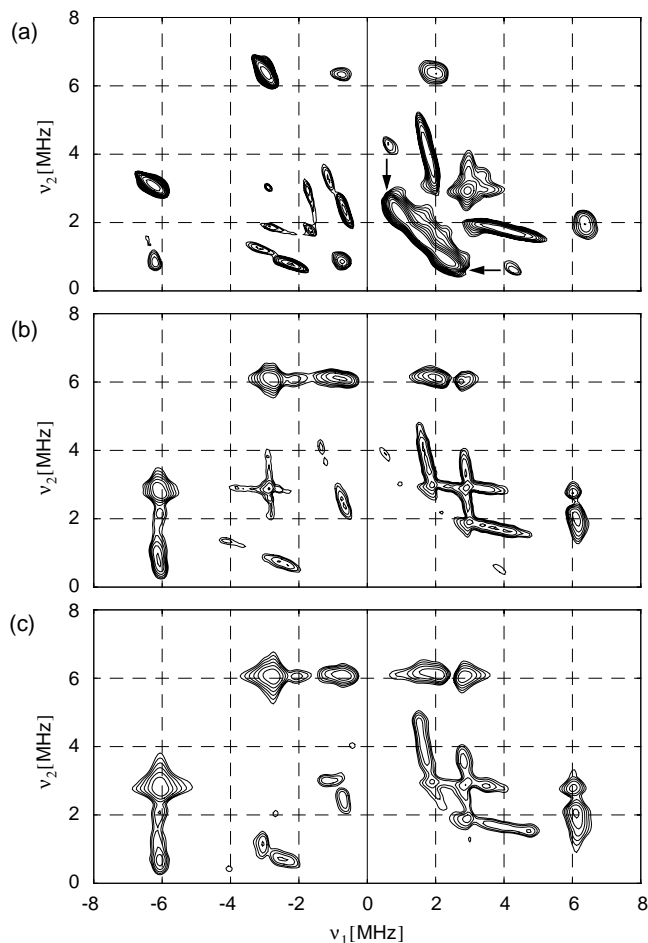

FIG. 6. HYSCORE spectrum of (oxyCo)[^{15}N]TPP(py) at $B_0 = 342.0$ mT. (a) Experimental spectrum. Arrows indicate the peaks assigned to the ^{15}N nuclei of the porphyrin ligand. (b) Corresponding simulated HYSCORE spectrum (^{14}N nucleus of the pyridine) assuming ideal pulses of zero length. (c) Simulation with pulses of finite length, $t_{\pi/2} = 24$ ns and $t_\pi = 16$ ns.

sides the signal arising from the interactions with the ^{15}N nuclei of the porphyrin ligand (arrows in Fig. 6a), a number of cross peaks are observed which can be assigned to the interaction with the ^{14}N nucleus of the pyridine ligand.

Figure 6b shows the corresponding simulated HYSCORE spectrum obtained using the following parameters: $g_x = 2.002$, $g_y = 1.9827$, and $g_z = 2.0705$; $A_x^{Co} = -53$ MHz, $A_y^{Co} = -21.4$ MHz, and $A_z^{Co} = -22.7$ MHz; $A_x^N = 3.4$ MHz, $A_y^N = 3.4$ MHz, and $A_z^N = 3.7$ MHz; $(e^2qQ)/h = 2.95$ MHz, $\eta = 0.23$, and $\beta = 65°$, and assuming ideal pulses. The interaction with the ^{15}N nuclei of the porphyrin ligand is not taken into account. A superposition of a total of 18,000 HYSCORE experiments with different orientations and electron Zeeman frequency offsets was included in the final time-domain simulation with 128×128 data points. The required computer time was approximately 46 min using GAMMA and 20 min using MATLAB on a SUN SPARC Ultra 10 computer with

300 MHz clock frequency and 256 MB main memory. The simulation reflects largely the features from the experimental HYSCORE spectrum. Using the algorithm described in the above-mentioned frequency-domain simulations an overview of all the possible frequencies in the HYSCORE spectrum may be obtained in less than 1 min on the same computer when including only 1800 different orientations in the calculation. Figure 6c shows the HYSCORE spectrum simulated with identical spin system parameters but using finite length pulses with $t_{\pi/2} = 24$ ns and $t_\pi = 16$ ns. The similarity between the two spectra of Figs. 6b and 6c also indicates that the use of ideal pulses in the simulation is justified at frequencies smaller than approximately 10 MHz.

Although the ESEEM techniques can in principle be used to observe interactions with any nuclear spin $I \geq 1/2$, experimental ESEEM spectra of $I > 1$ systems are scarce (56–60). Since several relevant nuclei have a spin larger than 1 ($I = 3/2$: ^{7}Li, ^{9}Be, ^{11}B, ^{23}Na, ^{33}S, ^{35}Cl, ^{37}Cl, ^{39}K, ^{61}Ni, ^{63}Cu, ^{65}Cu, ^{79}Br, ^{81}Br, ^{87}Rb; $I = 5/2$: ^{17}O, ^{25}Mg, ^{27}Al, ^{55}Mn, ^{47}Ti, ^{85}Rb, ^{127}I; $I = 3$: ^{10}B; $I = 7/2$: ^{49}Ti, ^{51}V, ^{59}Co), the lack of ESEEM data on $S = 1/2$, $I > 1$, systems must be due to the complexity of the experimental spectra. In Fig. 7a we show the experimental single-crystal HYSCORE spectrum of RbCl : O$_2^-$ taken at an observer position close to the [110] axis (g_z axis). The O$_2^-$ defect in RbCl has been studied extensively using continuous wave ENDOR (55). O$_2^-$ replaces a single Cl$^-$ ion in the crystal lattice and interacts with six neighboring Rb nuclei. The largest hyperfine interaction (interaction 1) is caused by the four nearest neighboring Rb ions in the (001) plane, whereas the interaction of the two Rb nuclei along the [001] axis with the unpaired electron is weaker (interaction 2). Rubidium has two isotopes: ^{85}Rb ($I = 5/2$, natural abundance 72.17%) and ^{87}Rb ($I = 3/2$, natural abundance 27.83%). The HYSCORE spectrum looks indeed complicated as can be appreciated from Fig. 7a. Simulations using the ^{85}Rb ENDOR data (55) revealed, however, that only the interactions with the ^{85}Rb nuclei are visible in the HYSCORE spectra.

Figure 7b shows the simulated HYSCORE spectrum with one of the four equatorial Rb nuclei ($g_x = 1.9836$, $g_y = 1.9846$, and $g_z = 2.2947$; Rb interaction 1: $A_{x'} = 11.49$ MHz, $A_{y'} = 6.52$ MHz, $A_{z'} = 6.3$ MHz, $\angle(A_{x'}, g_x) = 39.8°$; $Q_{x''} = 0.33$ MHz, $Q_{y''} = -0.23$ MHz, $Q_{z''} = -0.1$ MHz, $\angle(Q_{x''}, g_x) = 78.7°$; (55)). At the observer position, the hyperfine coupling $A(g_z)$ is 8.8 MHz. Since the ^{85}Rb Zeeman frequency amounts only to 1.25 MHz at this magnetic field position, the strong-coupling case ($|A(g_z)| > 2\nu_{Rb}$) applies (1), which explains why the largest signal intensity is found in the $(-, +)$ quadrant of the spectrum. As shown in Fig. 7b, the cross peaks between the five basic frequencies of the α and the β electron spin manifold, $(-\nu_{SQ(i)}^\alpha, \nu_{SQ(i)}^\beta)$ and $(-\nu_{SQ(i)}^\beta, \nu_{SQ(i)}^\alpha)$, with $i = 1$ to 5, are approximately centered around $(-4.4 \text{ MHz}, 4.4 \text{ MHz})$ ($A(g_z)/2 = 4.4$ MHz). The fact that only 8 instead of 10 cross peaks are visible results from an accidental overlap of $(-\nu_{SQ(3)}^\alpha, \nu_{SQ(3)}^\beta)$ and $(-\nu_{SQ(5)}^\beta, \nu_{SQ(5)}^\alpha)$ as is indicated in Fig. 7b. Furthermore, cross
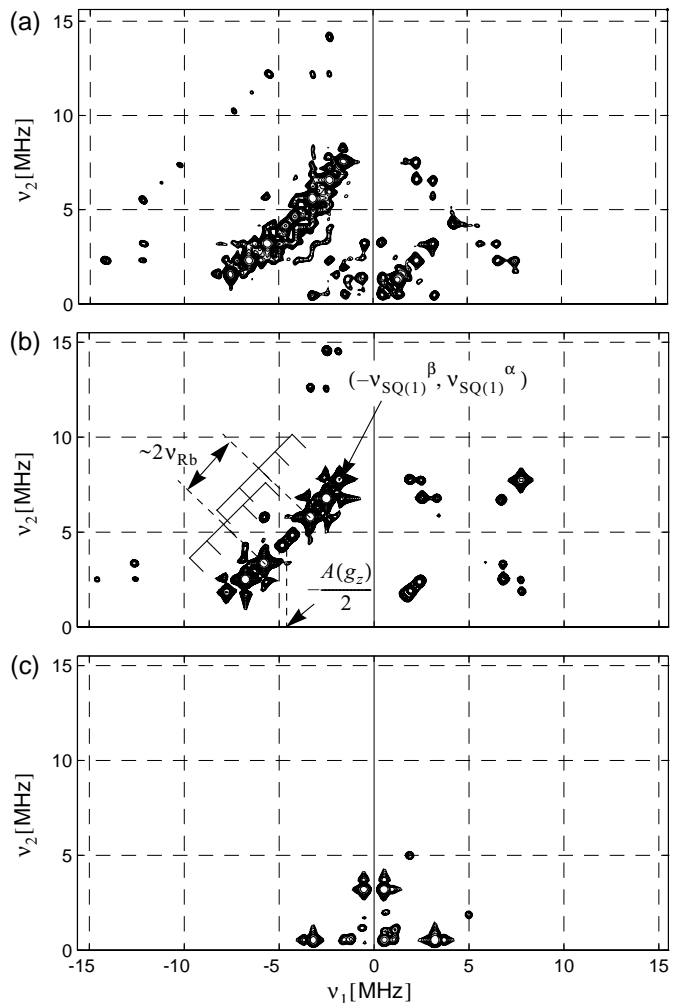

FIG. 7. HYSCORE of RbCl:O$_2^-$. (a) Experimental spectrum of a RbCl:O$_2^-$ single crystal at an observer position near the [110] axis ($B_0 = 302.9$ mT). (b) Simulation of the HYSCORE signals of the equatorial ^{85}Rb interaction at this observer position (parameters, see text). (c) Simulation of the HYSCORE signals of the axial ^{85}Rb interaction at this observer position (parameters, see text).

peaks between the DQ and SQ frequencies are observed in the $(-, +)$ quadrant of the HYSCORE spectrum.

Figure 7c shows the simulated HYSCORE spectrum for the interaction with one of the axial Rb nuclei (Rb interaction 2: $A_x = -1.53$ MHz, $A_y = -1.16$ MHz, $A_z = -1.63$ MHz; $Q_x = 0.09$ MHz, $Q_y = 0.21$ MHz, $Q_z = -0.3$ MHz). In the case of exact cancellation ($|A| = 2\nu_{Rb}$), the effective field experienced by the nucleus in one of the two m_S manifolds is approximately zero. The ESEEM frequencies within this manifold are then close to the two true nuclear quadrupole resonance frequencies expected for an $I = 5/2$ nucleus. Interaction 2 is near the cancellation condition ($|A_z| \approx 2\nu_{Rb}$), but the situation is complicated by the fact that $|3Q_z| \approx |A_z/2| \approx \nu_{Rb}$, so that in the β manifold one of the nuclear frequencies is close to zero. This has a significant influence on the nuclear transition probabilities, and combined with the fact that $|A_z/2| = 0.815$ MHz is

slightly smaller than ν_{Rb}, this explains why the HYSCORE features in Fig. 7c are not interpretable in a straightforward way. However, the possibility of simulating the HYSCORE spectra of complicated $S = 1/2$, $I > 1$ systems opens a way to the understanding of the different signals observed in these spectra.

CONCLUSION

In cases when no analytical formulae for the calculation of an echo modulation exist, numerical simulation based on the density operator formalism is a valuable method for calculating one- and two-dimensional ESEEM spectra. In this work it is shown how both single crystals and disordered systems can be treated. An attempt was made to address experimental imperfections such as field inhomogeneities and finite mw power. Experimental and simulated spectra show acceptable qualitative agreement. The number of spins included is limited only by the available computer time and memory. Simulations in both the time and the frequency domain represent efficient and complementary approaches for the calculation of pulse EPR spectra. Moreover, simulations make a theoretical study of complex features appearing in HYSCORE spectra of $S = 1/2$, $I > 1$ systems feasible.

Requests for the programs described in this article are to be addressed to the authors.

ACKNOWLEDGMENTS

REFERENCES

1. A. Schweiger and G. Jeschke, "Principles of Pulse Electron Paramagnetic Resonance," Oxford Univ. Press, Oxford (2001).

2. S. A. Dikanov and Yu. D. Tsvetkov, "Electron Spin Echo Envelope Modulation (ESEEM) Spectroscopy," CRC Press, Boca Raton, FL (1992).

3. A. Schweiger, *Angew. Chem. Int. Ed. Engl.* **30,** 265 (1991).

4. Y. Deligiannakis, M. Louloudi, and N. Hadjiliadis, *Coord. Chem. Rev.* **204,** 1 (2000).

5. P. Höfer, A. Grupp, H. Nebenführ, and M. Mehring, *Chem. Phys. Lett.* **132,** 279 (1986).

6. MATLAB v. 5.3, The MathWorks, Inc., Natick, MA.

7. IDL v. 5, Research Systems, Inc., Boulder, CO.

8. Mathematica 4.0, Wolfram Research, Inc., Champaign, IL.

9. H. Lee, P. E. Doan, and B. M. Hoffman, *J. Magn. Reson.* **140,** 91 (1999).

10. M. Romanelli and L. Kevan, *J. Chem. Phys.* **86,** 4369 (1986).

11. M. Romanelli, D. Goldfarb, and L. Kevan, *Mag. Reson. Rev.* **13,** 179 (1988).

12. L. Kevan, Developments in electron spin-echo-modulation analysis, *in* "Modern Pulsed and Continuous-Wave Electron Spin Resonance" (L. Kevan and M. K. Bowman, Eds.), p. 231, Wiley, New York (1990).

13. A. M. Prakash and L. Kevan, *J. Phys. Chem. B* **103,** 2214 (1999).

14. M. A. Djieugoue, A. M. Prakash, Z. D. Zhu, and L. Kevan, *J. Phys. Chem. B* **103,** 7277 (1999).

15. C. P. Keijzers, E. J. Reijerse, P. Stam, M. F. Dumont, and M. C. M. Gribnau, *J. Chem. Soc. Faraday Trans. I* **83,** 3493 (1987).

16. N. P. Benetis and A. R. Sornes, *Concepts Magn. Reson.* **12,** 410 (2000).

17. R. Szosenfogel and D. Goldfarb, *Mol. Phys.* **95,** 1295 (1998).

18. A. Pöppl and L. Kevan, *J. Phys. Chem.* **100,** 3387 (1996).

19. A. Pöppl, M. Hartmann, W. Böhlmann, and R. Böttcher, *J. Phys. Chem. A* **102,** 3599 (1998).

20. A. Pöppl, M. Gutjahr, M. Hartmann, W. Böhlmann, and R. Böttcher, *J. Phys. Chem. B* **102,** 7752 (1998).

21. R. R. Ernst, G. Bodenhausen, and A. Wokaun, "Principles of NMR in One and Two Dimensions," Clarendon, Oxford (1987).

22. P. Hodgkinson and L. Emsley, *Prog. Nucl. Magn. Reson. Spectrosc.* **36,** 201 (2000).

23. M. Bak, J. T. Rasmussen, and N. Chr. Nielsen, *J. Magn. Reson.* **147,** 296 (2000).

24. S. A. Smith, T. O. Levante, B. H. Meier, and R. R. Ernst, *J. Magn. Reson.* **106,** 75 (1994).

25. M. Willer and A. Schweiger, *Chem. Phys. Lett.* **230,** 67 (1994).

26. G. Jeschke and A. Schweiger, *Mol. Phys.* **88,** 355 (1996).

27. A. Ponti, *J. Magn. Reson.* **127,** 87 (1997).

28. S. Van Doorslaer and A. Schweiger, *Chem. Phys. Lett.* **281,** 297 (1997).

29. C. P. Slichter, "Principles of Magnetic Resonance," 3rd ed., Springer-Verlag, Berlin (1996).

30. K. Blum, "Density Matrix Theory and Applications," Plenum, New York (1981).

31. W. B. Mims, *Phys. Rev. B* **5,** 2409 (1972).

32. J. J. Shane, L. P. Liesum, and A. Schweiger, *J. Magn. Reson.* **134,** 72 (1998).

33. R. P. J. Merks and R. de Beer, *J. Phys. Chem.* **83,** 3319 (1979).

34. G. Jeschke and A. Schweiger, *J. Chem. Phys.* **106,** 9979 (1997).

35. C. Gemperle, Ph.D. thesis, ETH Zürich, No. 9192 (1990).

36. A. Pöppl, R. Böttcher, and G. Völkel, *Appl. Magn. Reson.* **12,** 15 (1997).

37. A. Ponti, *J. Magn. Reson.* **138,** 288 (1999).

38. G. Rist and J. Hyde, *J. Chem. Phys.* **49,** 2449 (1968).

39. G. Rist and J. Hyde, *J. Chem. Phys.* **52,** 4532 (1970).

40. G. Rist and J. Hyde, *J. Chem. Phys.* **52,** 4643 (1970).

41. B. M. Hoffman, J. Martinsen, and R. A. Ventres, *J. Magn. Reson.* **59,** 110 (1984).

42. B. M. Hoffman, R. A. Ventres, and J. Martinsen, *J. Magn. Reson.* **62,** 537 (1985).

43. G. C. Hurst, T. A. Henderson, and R. W. Kreilick, *J. Am. Chem. Soc.* **107,** 7294 (1985).

44. B. M. Hoffman and R. J. Gurbiel, *J. Magn. Reson.* **82,** 309 (1989).

45. M. J. Mombourquette and J. A. Weil, *J. Magn. Reson.* **99,** 37 (1992).

46. G. Jeschke and A. Schweiger, *J. Chem. Phys.* **105,** 2199 (1996).

47. G. Jeschke, R. Rakhmatulline, and A. Schweiger, *J. Magn. Reson.* **131,** 261 (1998).

48. L. P. Liesum, J. J. Shane, and A. Schweiger, "Magnetic Resonance and Related Phenomena," Vol. II, p. 1150, Technische Universität Berlin (1998).

49. L. Liesum and A. Schweiger, *J. Chem. Phys.* **114,** 9478 (2001).

50. G. Bar, A. Pöppl, S. Vega, and D. Goldfarb, *J. Magn. Reson.* **145,** 115 (2000).

51. S. Stoll and A. Schweiger, in preparation.

52. S. A. Dikanov, L. Xun, A. B. Kerpiel, A. M. Tyrishkin, and N. K. Bowman, *J. Am. Chem. Soc.* **118,** 8408 (1996).

53. J. J. Shane, P. Höfer, E. J. Reijerse, and E. de Boer, *J. Magn. Reson.* **99,** 596 (1992).

54. S. Van Doorslaer and A. Schweiger, *J. Phys. Chem. B* **104,** 2219 (2000).

55. S. Van Doorslaer, F. Callens, F. Maes, and E. Boesman, *Phys. Rev. B* **51,** 12480 (1995).

56. L. Astrakas, Y. Deligiannakis, G. Mitrikas, and G. Kordas, *J. Chem. Phys.* **109,** 8612 (1998).

57. L. Astrakas and G. Kordas, *J. Chem. Phys.* **110,** 6871 (1999).

58. K. Exner, O. Cullman, M. Vöglte, H. Prinzbach, B. Grossman, J. Heinze, L. P. Liesum, R. Bachmann, A. Schweiger, and G. Gescheidt, *J. Am. Chem. Soc.* **122,** 10650 (2000).

59. G. Jeschke, M. Kroschel, and M. Jansen, *J. Non-Cryst. Solids* **260,** 216 (1999).

60. G. Kordas, *J. Non-Cryst. Solids* **260,** 75 (1999).